ADVANCES IN ATMOSPHERIC SCIENCES, VOL. 24, NO. 1, 2007, 65–81

A Heavy Sea Fog Event over the Yellow Sea in March 2005: Analysis and Numerical Modeling

GAO Shanhong*[1] (高山红), LIN Hang[2] (林 行), SHEN Biao[1] (沈 飙), and FU Gang[1] (傅 刚)

[1] *Physical Oceanography Laboratory, Ocean University of China, Qingdao* 266003

[2] *Qingdao Meteorology Observatory, Qingdao* 266003

(Received 19 October 2005; revised 30 May 2006)

ABSTRACT

In this paper, a heavy sea fog episode that occurred over the Yellow Sea on 9 March 2005 is investigated. The sea fog patch, with a spatial scale of several hundred kilometers at its mature stage, reduced visibility along the Shandong Peninsula coast to 100 m or much less at some sites. Satellite images, surface observations and soundings at islands and coasts, and analyses from the Japan Meteorology Agency (JMA) are used to describe and analyze this event. The analysis indicates that this sea fog can be categorized as advection cooling fog. The main features of this sea fog including fog area and its movement are reasonably reproduced by the Fifth-generation Pennsylvania State University/National Center for Atmospheric Research Mesoscale Model (MM5). Model results suggest that the formation and evolution of this event can be outlined as: (1) southerly warm/moist advection of low-level air resulted in a strong sea-surface-based inversion with a thickness of about 600 m; (2) when the inversion moved from the warmer East Sea to the colder Yellow Sea, a thermal internal boundary layer (TIBL) gradually formed at the base of the inversion while the sea fog grew in response to cooling and moistening by turbulence mixing; (3) the sea fog developed as the TIBL moved northward and (4) strong northerly cold and dry wind destroyed the TIBL and dissipated the sea fog. The principal findings of this study are that sea fog forms in response to relatively persistent southerly warm/moist wind and a cold sea surface, and that turbulence mixing by wind shear is the primary mechanism for the cooling and moistening the marine layer. In addition, the study of sensitivity experiments indicates that deterministic numerical modeling offers a promising approach to the prediction of sea fog over the Yellow Sea but it may be more efficient to consider ensemble numerical modeling because of the extreme sensitivity to model input.

Key words: sea fog, Yellow Sea, numerical modeling, MM5, sensitivity experiments

DOI: 10.1007/s00376-007-0065-2

1. Introduction

Sea fog is a dangerous weather phenomenon over the ocean and costal areas. It is produced by suspended water droplets and it is characterized by the visibility falling below 1 km. In some cases, it forms as a stratus-lowering process and can thus be considered to be cloud in contact with the sea surface (Koračin et al., 2001). In other cases, the fog forms immediately above the sea surface and can expand vertically to form a cloud (Findlater et al., 1989). Some heavy events result in extremely low visibility—less than a few meters. It is responsible for a variety of perilous situations that affect maritime activities such as fishery operations and traffic. The probability of collisions between ships increases precipitously in the presence of fog. The prediction of sea fog has great economic value and contributes to maritime safety.

Lewis et al. (2004) reviewed the sea fog research in the United Kingdom and United States. Their historical perspective emphasized sea fog in the eastern Pacific Ocean and the Atlantic Ocean. In particular, two ocean areas have received much attention: one is the coast of northeast Scotland (Findlater et al., 1989; Ballard et al., 1991) and the other is the coast of California (Pilié, 1979; Leipper, 1994; Lewis et al., 2003). However, in China, Wang (1983) focused on the analyses of sea fog in the East Asia area. Among the seas of China, the Yellow Sea (shown in Fig. 1) experiences sea fog most frequently, especially during the spring

*E-mail: gaosh@mail.ouc.edu.cn

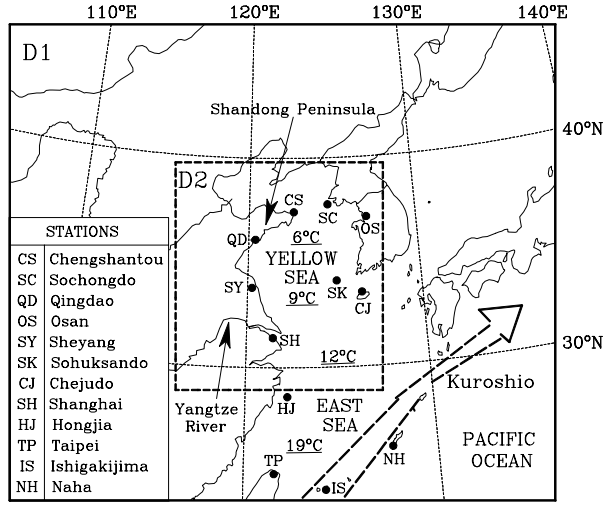

Fig. 1. Locations of weather reporting stations in this study. The SST on 9 March of different sea areas are presented, and the two squares marked with D1 and D2 respectively show the domains used for MM5 modeling later.

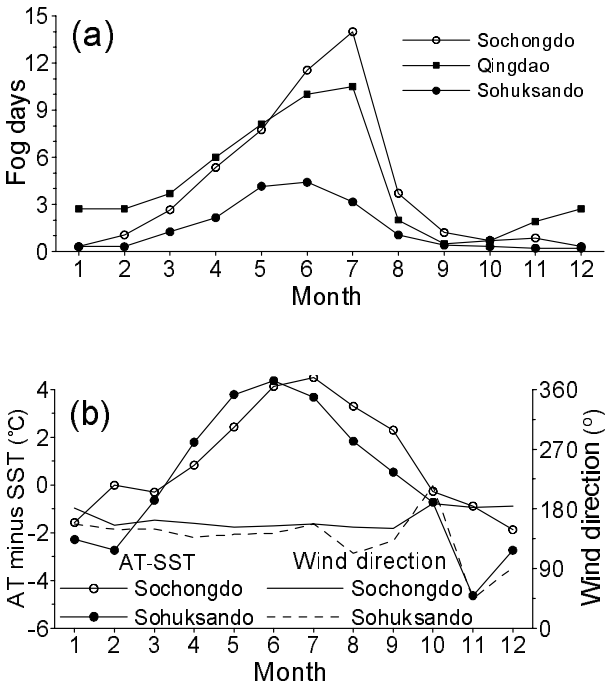

Fig. 2. Seasonal variation of sea fog occurrence at (a) SC, QD and SK, and (b) mean AT minus SST and wind direction at SC and SK. The stations are identified on the insert of Fig. 1.

and summer seasons. There exists a considerable body of work on the occurrence of sea fog over the Yellow Sea, among which are statistical studies of observations. Jing (1980) and Diao (1996) analysized the characteristics of sea fog along the coast of Qingdao. Zhao et al. (1997) classified weather patterns favorable for sea fog formation and development over the Yellow Sea using surface weather chart and Geostationary Meteorological Satellite (GMS-5) visible imagery. Utilizing the reanalysis data of the National Center for Atmospheric Research (NCAR), Zhou et al. (2004) studied the climatic characteristics of sea fog formation over the Yellow Sea in spring. Their work indicated that sea fog over the Yellow Sea has distinct monsoon characteristics where vapor transport from the tropical zone is a primary contributor to the fog formation.

As a complement to the previous statistical results of sea fog over the Yellow Sea, a long time series of observations recorded at three stations (Sohuksando, Qingdao, Sochongdo, see Fig. 1; period 1971–2000 for Qingdao and period 1983–2002 for the others) are utilized to investigate the seasonal variation of sea fog occurrence in different regions of the Yellow Sea and the oceanic and near-sea-surface atmospheric environment when sea fog occurs. Figure 2a shows that monthly mean sea fog frequency (fog days) is much higher in spring and summer than other seasons and increases with increasing latitude associated with decreasing sea surface temperature (SST). From Fig. 2b, it is clearly seen that sea surface winds come from the south and that atmospheric temperature (AT) is significantly warmer than SST (0°–4°C) during sea fog days in spring and summer. These observational results suggest that southerly winds and warm air moving over colder water play important roles in sea fog formation over the Yellow Sea during spring and summer.

Mixing (moistening and cooling) and radiative cooling are the main physical processes responsible for fog formation (Wang, 1983). Fog can be classified as advective when the first mechanism is prominent. Combined with previous studies, most sea fog over the Yellow Sea during spring and summer can be classified as advection fog, to be precise, the advection cooling fog. That is, the advection of warm air (formed over the ocean area with high SSTs) passing over a cold sea surface leads to the mixing of warm moist and conduction-cooled air producing saturation and fog. These processes were fundamentally explored by Taylor (1917) in the aftermath of the *Titanic* disaster. From a climatological view, the Yellow Sea is a favored place for sea fog because of its cold water and location adjacent to the warm Kuroshio Current (see Fig. 1) (Lewis et al., 2004).

Although efforts have been made to forecast these advection fog events over the Yellow Sea, the problem

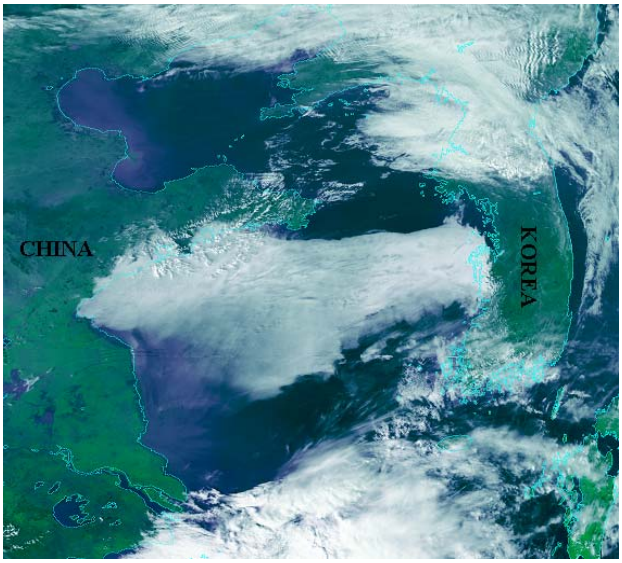

Fig. 3. Visible satellite imagery from NOAA-16 at 1400 LST 9 March 2005.

has proved most challenging. For instance, Hu et al. (1996) tried to predict sea fog along the South Shandong peninsula coast with a 24-h forecast lead time using statistical regression, and a similar method was used by Wang and Qu (1997) to forecast sea fog off the Qingdao coast. The applicability of these methods is limited to local region, because they rely on a few synoptic variables and local surface observational factors. It is well known that the formation and evolution of sea fog involve complicated dynamic and microphysical processes. An ambitious goal is to employ numerical models to predict sea fog and to study the processes affecting sea fog formation and evolution. Ballard et al. (1991) were the first to attempt sea fog prediction using a regional mesoscale model. Hu and Zhou (1997) studied air-sea conditions affecting sea fog with a two-dimensional numerical model. However, many numerical modeling studies of fog (Ballard et al., 1991; Bergot and Guedalia, 1994; Pagowski et al., 2004) pointed out that there are potential difficulties in fog modeling and prediction, such as the lack of accurate initial humidity and temperature profiles in the boundary layer (particularly over vast ocean without observations), and the uncertainties in the parameterization of microphysics, turbulence and radiation, etc. Fortunately, with the rapid progress of numerical models and increasing observations, there is hope that the dynamical prediction of sea fog will become viable in the near future.

Within the past decade (1990s–2000s), a number of numerical simulations of sea fog over the Yellow Sea have been completed. Fu et al. (2002) simulated a sea fog event over the Yellow Sea using a three-dimensional atmospheric boundary layer model. Fu et al. (2004) also employed the Regional Atmospheric Modeling System (RAMS) to simulate an extremely dense sea fog case over the Yellow Sea in April 2004, and they succeeded in reproducing the main features of this sea fog episode, such as fog area and its vertical structure. The fifth-generation Pennsylvania State University/NCAR mesoscale model (MM5) (Grell et al., 1994) includes several cloud microphysical process schemes employing cloud water as a prognostic variable, as well as cloud ice, and it is suitable for studying sea fog. Fan et al. (2003) utilized the MM5 model to successfully simulate an advection fog event that occurred in the Nanling Mountain area of South China; Pagowski et al. (2004) also used the MM5 model with very high resolution (1 km) to carefully study an extremely dense fog with a spatial scale of several kilometers.

In this paper, the MM5 model will be employed to investigate a heavy sea fog event over the Yellow Sea on 9 March 2005 with the goal to better understand its formation and evolution. We then explore the possibility of forecasting sea fog over the Yellow Sea by numerical models. In the following sections, the sea fog case is synoptically analyzed in detail using observations. Then the ability of the MM5 model to capture the main observed features and evolution of this sea fog episode is assessed. Additionally, the sensitivity of the modeling result to horizontal and vertical resolutions, SSTs, schemes of planetary boundary layer (PBL) and initial conditions is discussed with a series of experiments. Finally, we present our conclusions.

2. Overview and analysis of the sea fog episode

2.1 *Case overview*

A heavy sea fog event occurred over the Yellow Sea on 9 March 2005. Figure 3 shows the high-resolution visible image at 1400 local standard time (LST, UTC +8 h) on 9 March from the National Oceanic and Atmospheric Administration satellite (NOAA-16). A large area of sea fog occurs over much of the Yellow Sea. This patch can be identified as fog due to the whiteness of the image with smooth texture and distinct edges. This fog patch is also clearly recognized from the infrared image of NOAA-16 at the same time (not shown) with cloud ceiling brightness temperature (TBB) ranging from 2°C to 6.8°C. The height of the fog top over the Qingdao area is estimated to be approximately 400 m by comparing TBB with the temperature profile of sounding data from Qingdao station. The images of Geostationary Operational Environmental Satellite (GOES-9) in Fig. 4 illustrate the evolution of this fog. The sea fog formed in the South

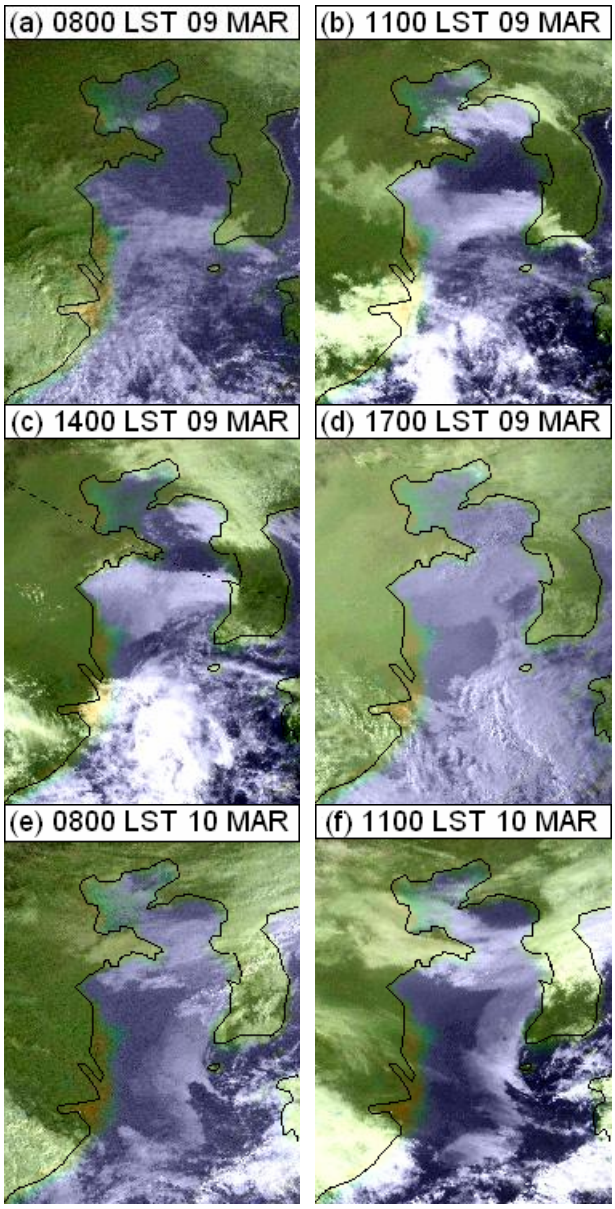

Fig. 4. Visible satellite imagery from GOES-9.

Yellow Sea at 0800 LST 9 March (Fig. 4a) and quickly moved northward. Three hours later, it occupied the West and South Yellow Sea (Fig. 4b). It matured at 1400 LST 9 March (Fig. 4c) and then slowly moved northward (Fig. 4d). Difficulty in the use of infrared imagery from satellites prevented us from identifying the fog during nighttime. On the morning of 10 March, the sea fog patch moved southward and started to dissipate, and a new smaller sea fog patch was generated over the Southeast Yellow Sea (Figs. 4e, f).

However, surface observations at coastal stations revealed that from the evening of 9 March the sea fog continued to move northward, intruded inland and resulted in very low visibility over land. The sea fog lasted about 18 h and 12 h at Qingdao and Chengshantou respectively, and sometimes near-zero visibility was observed at both stations (Figs. 5a, b). From Fig. 5, a close relationship is obviously seen between visibility and wind at Qingdao and Chengshantou, i.e., southerly wind prompted sea fog formation while northerly wind dissipated the sea fog. However, at Shanghai and Chejudo, southerly winds prevailed for a long time but no sea fog was observed (Figs. 5c, d).

2.2 *Case analysis*

For analyzing the physics of this sea fog episode, besides satellite images and surface observations mentioned above, sounding data and analyses from the World Meteorological Organization-Distributed Data Bases (WMO-DDBs) by the Japan Meteorology Agency (JMA) are used to provide the synoptic situation. SST data from the North-East Asian Regional Global Ocean Observing System (NEAR-GOOS) are also used.

The synoptic features that resided over the Yellow Sea during the period 8–11 March are depicted in the panels of Fig. 6. By viewing the surface winds in panels (a)–(c), it is clear that the surface air coming into the Yellow Sea region on 8–10 March had its roots far to the south. This air exhibited long over-water trajectories that stemmed from oceanic regions near Taiwan Island. In Fig. 6a, a warm front is indicated along the leading edge of this southerly flow. The ridge of high pressure south of Kyushu of Japan in combination with the low pressure over the eastern Chinese mainland governed this persistent southerly flow. The warm front coincided with a trough of low pressure that extended southwestward from the primary cyclone over Sakhalin. Examination of the synoptic sequence in Fig. 6 indicates that this cyclone moved eastward over the 3-day period. In association with the movement of this cyclone, the primary anticyclone over Mongolia moved southward and produced northerly winds over the Yellow Sea by 11 March (Fig. 6c, d). This cyclone/anticyclone couplet and its movement was the dominant large-scale feature that controlled the duration of the heavy sea fog event.

The southerly winds (advection) transported plenty of warm moist air onto the Yellow Sea, which can be judged from the moist tongue expanding northward (see the water vapor mixing ratio contour in Figs. 6a, b). Besides the warm moist advection, the SST of the Yellow Sea was much cooler (0°–6°C) than the near-sea-surface atmospheric temperature (seen from the distribution of the difference between AT and SST over the Yellow Sea, not shown). Compared with the sea fog patches in the GOES-9 visible images (Fig. 4)

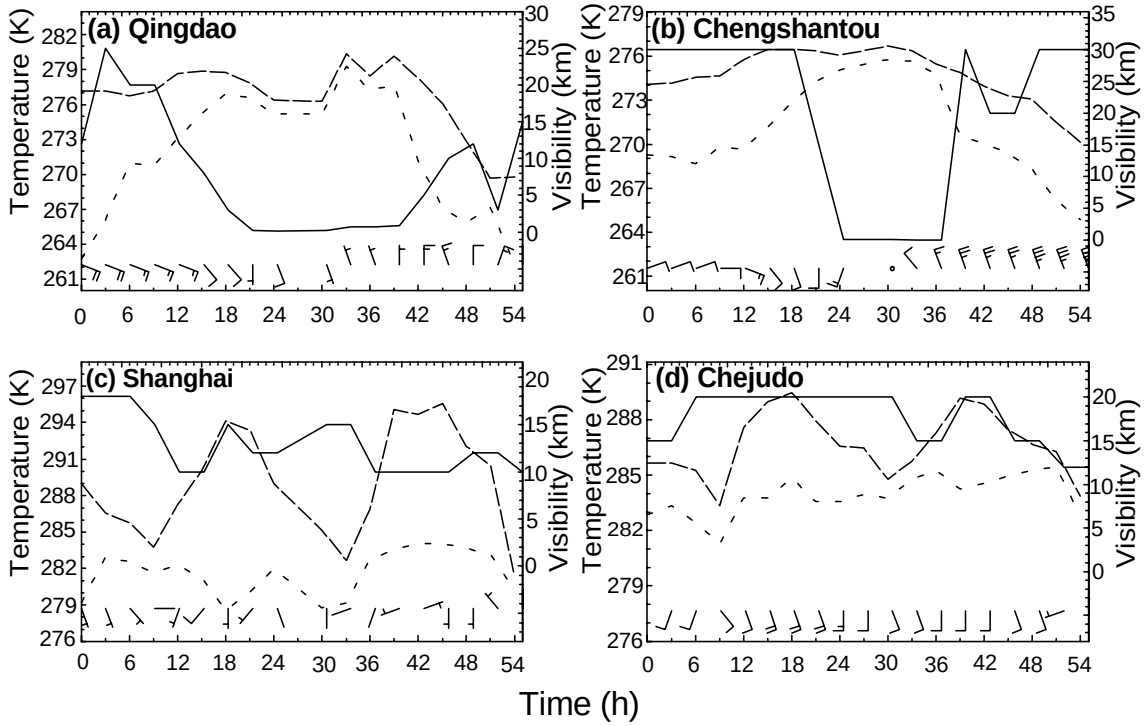

Fig. 5. Time series of surface observations at 4 stations surrounding the Yellow Sea (starting time: 0800 LST 08 March 2005, solid for visibility, long-dashed for temperature and short-dashed for dew point temperature, full barb at 5 m s^{-1}).

and the visibility observations along the Yellow Sea coast, AT minus SST between 0°–4°C was likely suitable for sea fog formation while too great AT minus SST was not. For example, there was high visibility at Shanghai but large AT minus SST (6°C) existed in the Yangtze estuary. This analysis result agrees with the observational statistics mentioned above (Fig. 2b) and others (Cho et al., 2000; Zhang et al., 2005).

The higher-level air retained a structure associated with the warming in the southern regions during 8–9 March. Figure 7 shows that high pressure controlled the whole East Sea and southwesterly winds dominated the Yellow Sea. This warming process can be obviously seen in Fig. 8. The warm moist southerly advection prompted the fog formation over the Yellow Sea on 9 March. However, the weather situation suitable for sea fog was maintained for no more than one day. On the backside of the disturbance, a very strong cold/dry anticyclone moved over the Yellow Sea (Figs. 6c, d) and mixed drier air with the fog layer to promote the sea fog dissipation. This change of synoptic regime is the main factor that usually destroys sea fog (Findlater et al., 1989; Lewis et al., 2003).

Figure 9 shows the variation of observed surface visibilities and the temperature profiles below 700 hPa at 6 stations that surround the Yellow Sea (see Fig. 1 for their locations). At 2000 LST 8 March, an inversion existed over the West Yellow Sea (see the profiles of Qingdao and Sheyang in Fig. 9a) and a light fog with 2-km visibility was observed at Sheyang. As time progressed, the area of inversion expanded and the inversion strengthened. In Fig. 9b, the inversion can also be found at Chengshantou, Shanghai and Osan, and the inversion at Qingdao and Sheyang became much stronger. Especially at Sheyang, strong inversion, exhibiting temperature increases of 10°C in about 250 m, reduced the visibility from 2 km to 200 m. At 2000 LST 9 March, dense sea fog with poor visibility (100 m or less) occurred at Chengshantou and Qingdao (Figs. 5a, b); similar to Sheyang at 0800 LST 9 March, the inversions appeared very strong and their bases were greatly lowered at these two stations. Meanwhile, at Sheyang, the inversion became much weaker and visibility increased as the sea fog moved northward (Fig. 4).

Taylor's original work (1917; reviewed by Lewis et al., 2004) showed the relationship of the inversion to surface conditions. In his research, he tracked the surface air movement for times of one week or more, and then he found that the air mass in the sea fog area came from the area with higher SST that was in evidence in the sounding data. We examined the soundings at Qingdao and Sheyang (Figs. 9a, b), then found that their profiles above inversion layers were quite si-

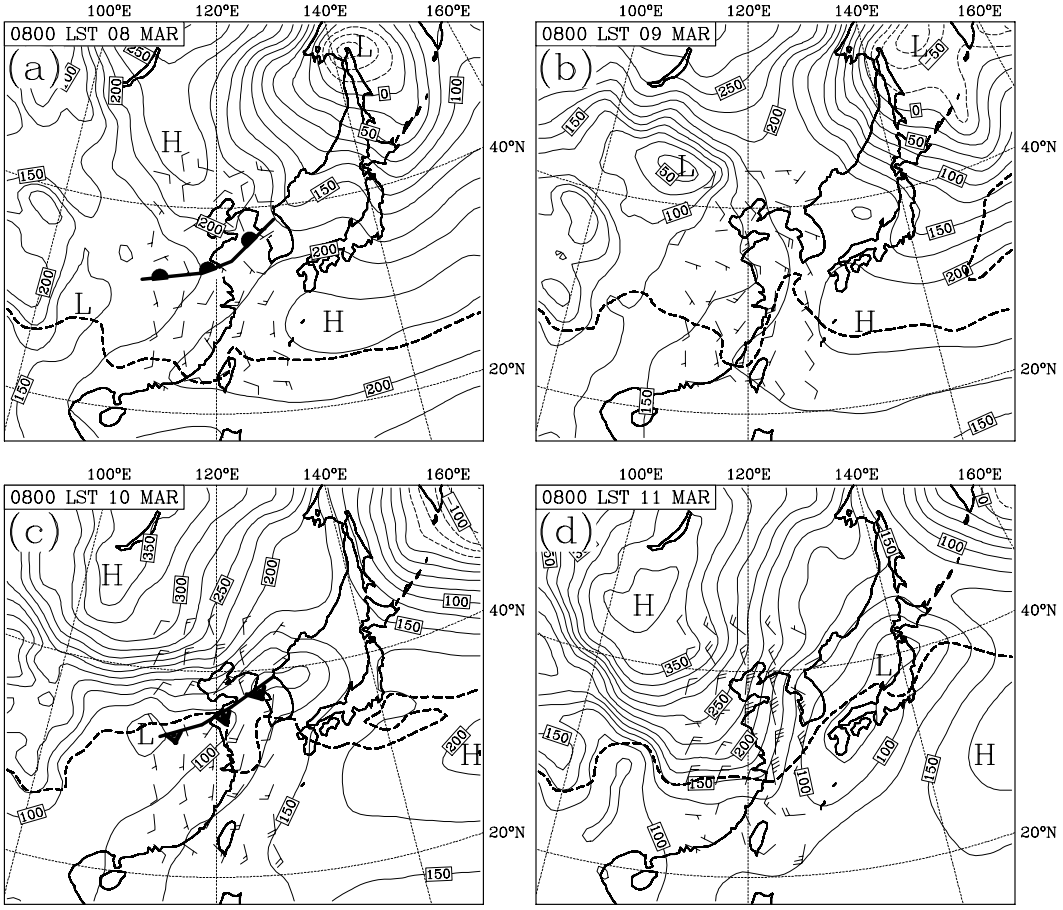

Fig. 6. Analyses of the 1000 hPa data from JMA at 0800 LST during 8–11 March. The coarse dashed line indicates the 7 $g\,kg^{-1}$ water vapor mixing ratio contour.

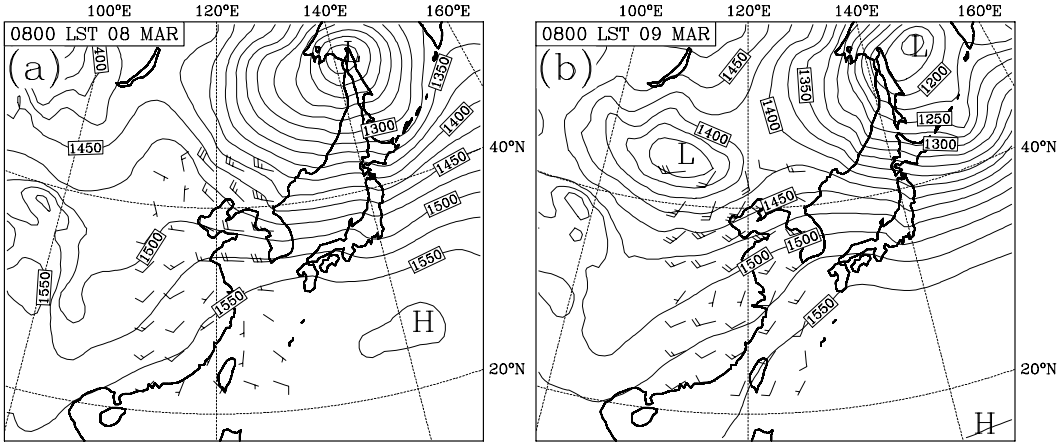

Fig. 7. Analyses of the 850 hPa data from JMA at 0800 LST during 8–9 March.

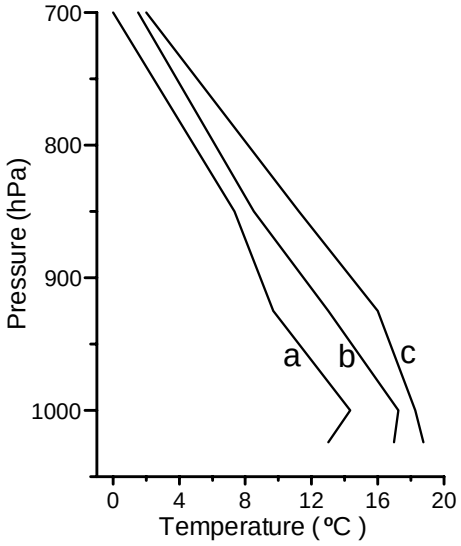

Fig. 8. Mean temperature vertical profiles of HJ, TP, IS and NH (see Fig. 1) at 0800 LST on the following days of March: 8 (a), 9 (b), and 10 (c).

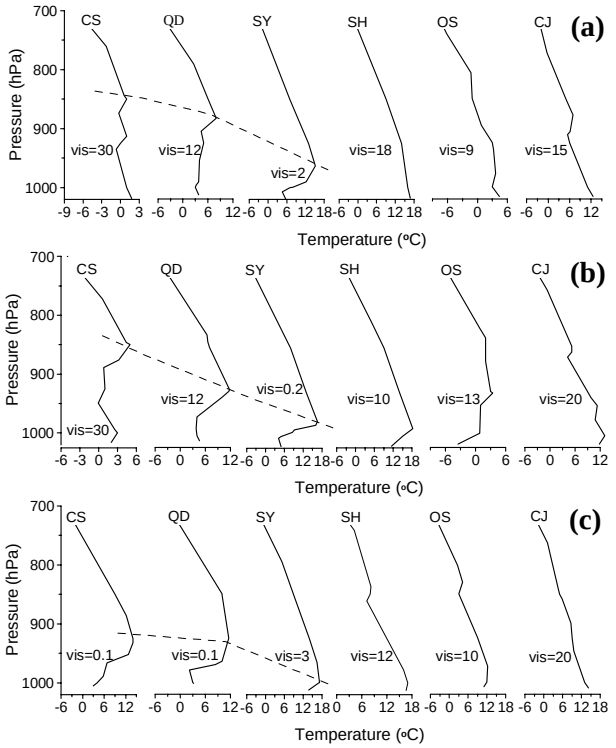

Fig. 9. Temperature profiles and visibilities (marked by "vis", in units of km) at the 6 stations surrounding the Yellow Sea at (a) 2000 LST 8 March 2005, (b) 0800 LST 9 March 2005 and (c) 2000 LST 9 March 2005. The stations are identified on the insert of Fig. 1.

milar, and that the extension of these soundings from the inversion layer top to the surface points at about 19°C, which was close to the SST near Taiwan Island (see Fig. 1). Therefore, it is hypothesized that the changes of the inversions at Sheyang, Qingdao and Chengshantou (see dashed lines in Fig. 9) are caused by the warm air mass moving from the south to the north.

We hope the following numerical modeling can reveal more details and then help us to better understand the formation and evolution of this sea fog.

3. Numerical modeling

3.1 *Data and modeling design*

The MM5 model (the non-hydrostatic version 3.7 with movable and multiple nesting grid) is employed in the present study. The data used to define MM5's initial and lateral conditions are the analyses from the WMO-DDBs by JMA. The data are 6-hourly with horizontal resolution 1.25° × 1.25° and 11 vertical levels from 1000 hPa to 100 hPa. These analyses are interpolated onto the model grids and are improved by incorporating observations through the use of a Cressman-type analysis scheme (Benjamin and Seaman, 1985). The observations are obtained from the Meteorological Information Composite and Processing System (MICAPS) of Qingdao Meteorology Observatory and include upper air soundings, surface observations and ship reports. These surface observations and ship reports also serve to validate the simulated results. Additionally, NEAR-GOOS daily SST data with a resolution of 0.25° × 0.25° are used.

Two domains with two-way nest interaction are designed. The Yellow Sea is wholly covered by the inner domain (see Fig. 1). The two domains have a horizontal grid-size of 36 km and 12 km with grid numbers of 80×70 and 91×100, respectively. The domain has 40 unevenly spaced full-sigma levels in the vertical with the high resolution in the boundary layer (20 levels below 850 hPa, with the first wind, humidity and temperature level at about 9 m).* The model top is 100 hPa. In order to prevent gravity waves from being reflected off the model top, Klemp and Durran (1983) upper-radiative boundary condition is applied. Meanwhile the sponge lateral boundary condition is used

*The sigma values are 1.0000, 0.9975, 0.9925, 0.9850, 0.9775, 0.9700, 0.9600, 0.9500, 0.9400, 0.9300, 0,9200, 0.9100, 0.9000, 0.8975, 0.8850, 0.8725, 0.8600, 0.8475, 0.8350, 0.8225, 0.8100, 0.7900, 0.7800, 0.7600, 0.7400, 0.7100, 0.6700, 0.6200, 0.5600, 0.5000, 0.4500, 0.4000, 0.3500, 0.3000, 0.2500, 0.2000, 0.1500, 0.1000, 0.0500 and 0.0000. Their corresponding heights are approximately as follows: 0, 9, 37, 83, 139, 196, 261, 337, 414, 491, 569, 648, 727, 778, 838, 939, 1041, 1145, 1250, 1355, 1462, 1603, 1735, 1869, 2050, 2283, 2618, 3068, 3650, 4331, 5005, 5666, 6382, 7164, 8027, 8991, 10086, 11359, 12887, 14816 m.

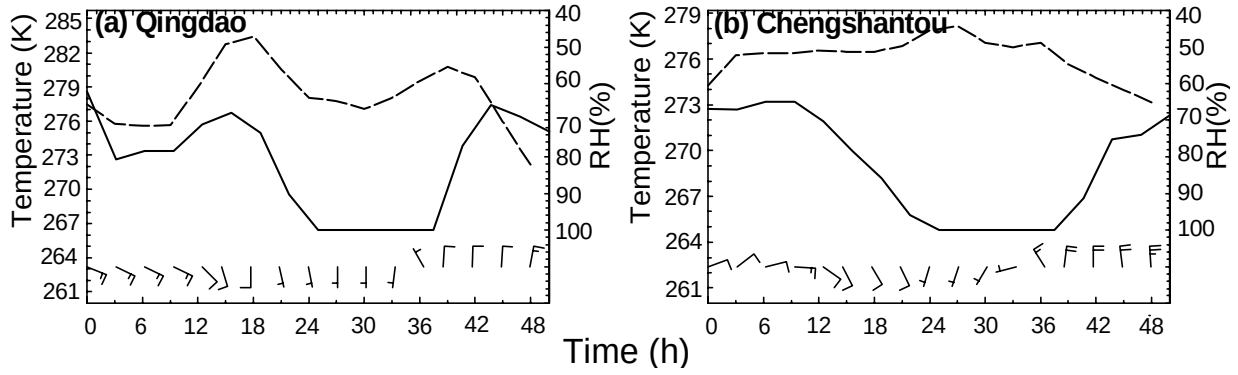

Fig. 10. Time series of simulated surface temperatures (dashed), relative humidities (RH, solid) and winds at Qingdao and Chengshantou (starting time: 0800 LST 08 March 2005).

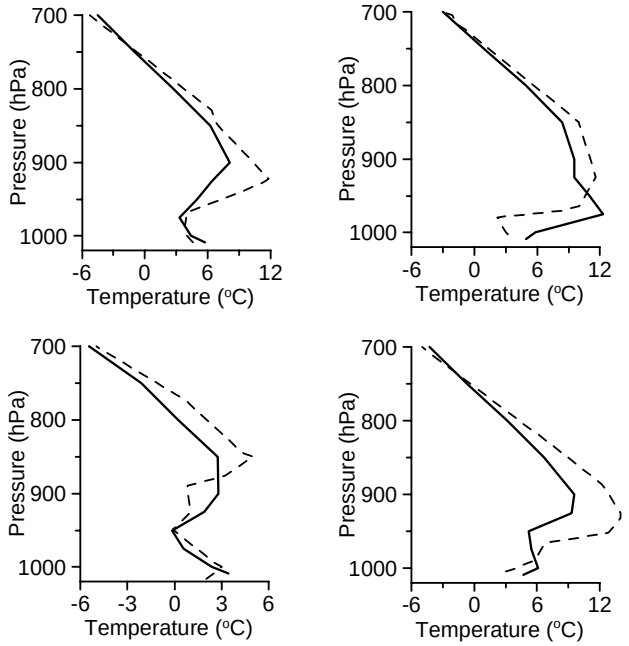

Fig. 11. Comparison of simulated (solid) and observed (dashed) temperature profiles at 0800 LST (left) and 2000 LST (right) on 9 March at Qingdao (upper) and Chengshantou (lower).

(Anthes et al., 1987).

Identical physical options apply to both domains. Reisner's graupel scheme is applied which is based on the mixed-phase scheme but it adds the graupel and ice number concentration prediction equations (Reisner et al., 1998). Grell cumulus parameterization (Grell et al., 1994) and the RRTM longwave radiation scheme combined with the cloud-radiation shortwave scheme (Dudhia, 1989) are used. The Rapid Radiative Transfer Model (RRTM) longwave scheme is a new, highly accurate and efficient method provided by AER Inc. (Mlawer et al., 1997). The planetary boundary layer (PBL) is parameterized by the high-resolution Hong-Pan scheme (Hong and Pan, 1996) and moist vertical diffusion is added to it. Since no extra soil data are provided in the JMA analyses and as land is relatively not as important as ocean in this sea fog case, the five-layer soil model (Dudhia, 1996) is employed instead of a land surface model. SST is permitted to vary in time during modeling, i.e. daily SST data are interpolated onto every time step.

3.2 *Control experiment*

The simulation period of numerical modeling is from 2000 LST 8 March to 2000 LST 10 March 2005 (48 h). Four-dimensional data assimilation (Newtonian relaxation approach) is performed during the first 12 h of the integration. This incorporates detail into the meteorological fields. Output is produced every 1 h for both domains, but we focus only on the result from the inner domain.

An evaluation is conducted to examine the model result. Firstly, the simulated 6-hourly synoptic situations at 1000 hPa, 850 hPa and 700 hPa are compared with the JMA analyses, and it is found that they are very similar and their differences are quite small (figures not shown). Secondly, the model output is interpolated at two selected stations (Qingdao and Chengshantou) to show a few details of the result. Figure 10 shows time series of simulated surface temperatures, relative humidities and winds at these stations, and Fig. 11 presents temperature vertical profiles of both the simulated and the observed. Contrasting Fig. 10 and Figs. 5a, b shows that the simulated surface winds agree with the observed and that the changes of temperature and relative humidity follow well the observed (100% relative humidity means fog with visibility less than 1 km). In Fig. 11, the strength of the simulated inversions at the two selected stations are relatively weak compared with the observed, however, their patterns and changes are quite similar.

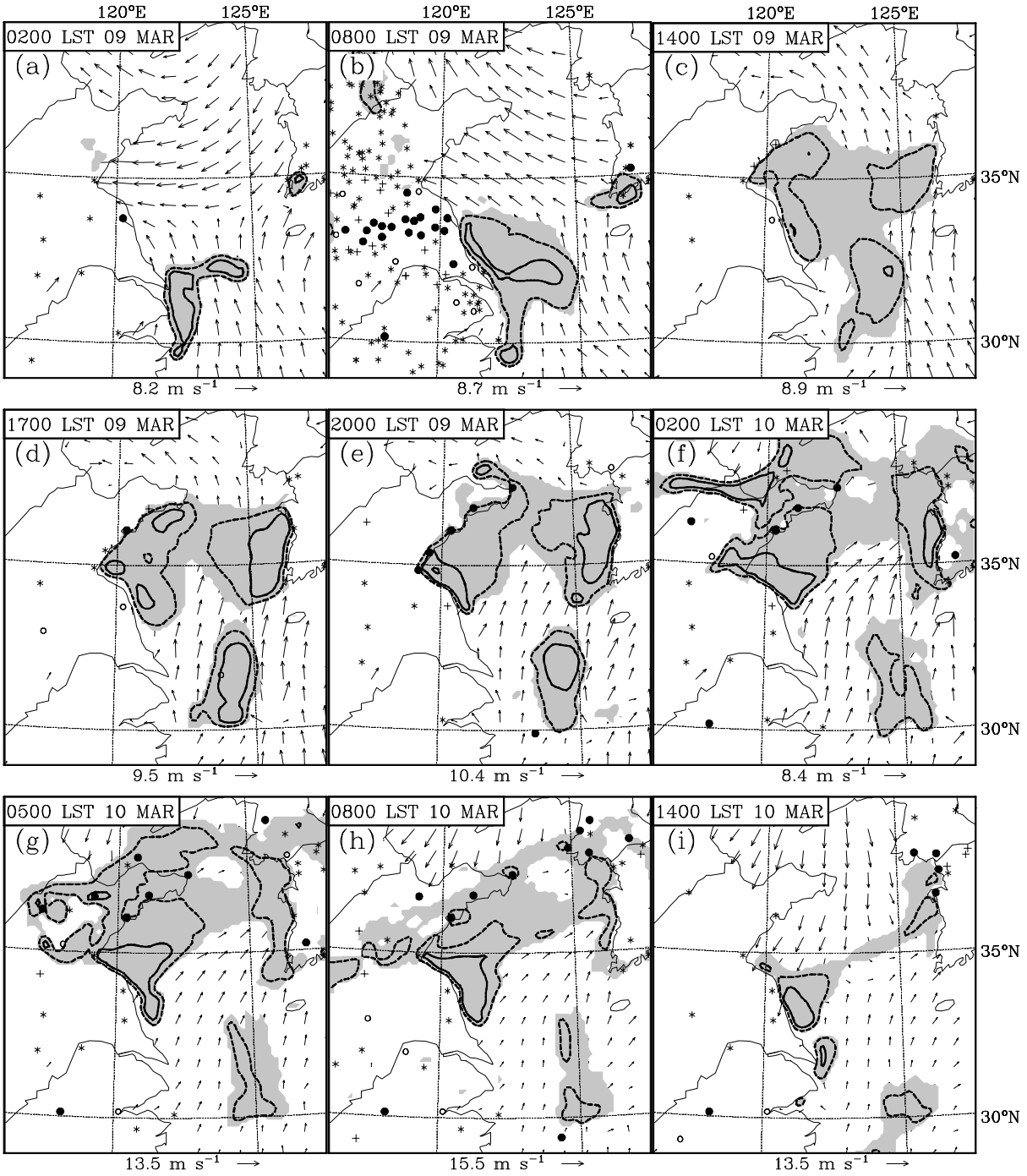

Fig. 12. Evolution of the simulated fog areas (shaded), cloud water mixing ratio at 10 m (contours; dashed at 0.3 g kg^{-1}, solid at 0.6 g kg^{-1}) and sea surface winds (vectors) in the control experiment. The symbols •, ∗, + and ∘ represent the observed visibility with values 0–1 km, 1–2 km, 2–3 km and 3–5 km respectively. The maximum vector is at the bottom of each picture.

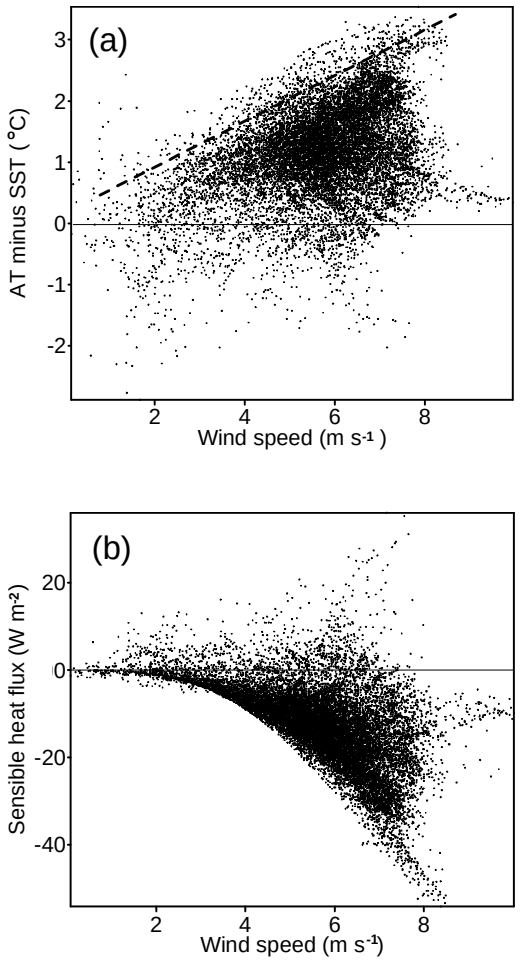

Fig. 13. Scatterplots of (a) AT minus SST vs. wind speed, and (b) sensible heat flux vs. wind speed during the sea fog forming and developing stages.

Based on the reasonable model result, we calculate the distribution of surface horizontal visibility in the inner domain in order to examine whether the MM5 model could capture the main features of the sea fog episode (i.e., fog area and its movement). This calculation uses the formula by Stoelinga and Thomas (1998) at 10 m above sea level, which is as follows:

$$x_{\rm vis} = -\ln(0.02)/\beta\,, \qquad (1)$$

where $x_{\rm vis}$ is the horizontal visibility (km) and β is the extinction coefficient ($\rm km^{-1}$). β is related to cloud liquid water, rain, cloud ice and snow. In this study, only cloud liquid water is considered because no precipitation and snow were observed and no model-produced cloud ice in low level atmosphere is found. The value of β is determined by the formula (Kunkel, 1984),

$$\beta = 144.7C^{0.88}\,, \qquad (2)$$

where C is the mass concentration of cloud liquid water ($\rm g\,m^{-3}$). Figure 12 displays the simulated fog area (the calculated visibility is less than 1 km). The sea fog began to form in the sea east of the Yangtze estuary after the midnight (2400 LST) of 8 March (Fig. 12a). With winds changing from easterly and northeasterly to southeasterly (Figs. 12b, c), the sea fog grew rapidly. A great large fog area appeared at 1400 LST 9 March (Fig. 12c), which indicates that the sea fog already matured. The high-resolution visible image in Fig. 3 shows that the sea fog is much denser over the western and eastern areas of the Yellow Sea. The distribution of cloud water mixing ratio in Fig. 12c embodies this fact. Pushed by southerly winds, the fog proceeded northward (Figs. 12d, e, f). But this displacement was terminated by the reverse of the winds. From 0500 LST 10 March onward, the winds changed from southwesterly to northeasterly and became rather strong (more than 13 $\rm m\,s^{-1}$) (Figs. 12g, h). Finally, the sea fog was almost destroyed by the cold and dry northerly winds (Fig. 12i). Comparing Fig. 12 with Fig. 4, it is clearly found that the forming, developing and dissipating stages are well duplicated by the model. For instance, the location and size of the sea fog patch are reasonably simulated (Fig. 12c vs. Fig. 4c, Fig. 12d vs. Fig. 4d and Fig. 12h vs. Fig. 4e, etc.). In particular, the movement of the sea fog patch is quite in accordance with visibility observations (as shown in Figs. 12c, d, e, etc).

In order to investigate the air-sea conditions during the sea fog forming and developing stages (from 2000 LST 8 March to 0200 LST 10 March), relationships of

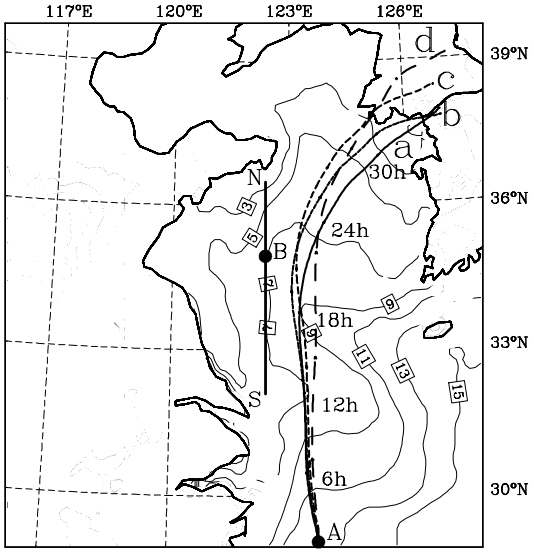

Fig. 14. Trajectories of air parcels starting from the location A at different heights: (a) 50 m, (b) 100 m, (c) 150 m and (d) 200 m. Contours indicate the NEAR-GOOS SST of the Yellow Sea on 9 March 2005.

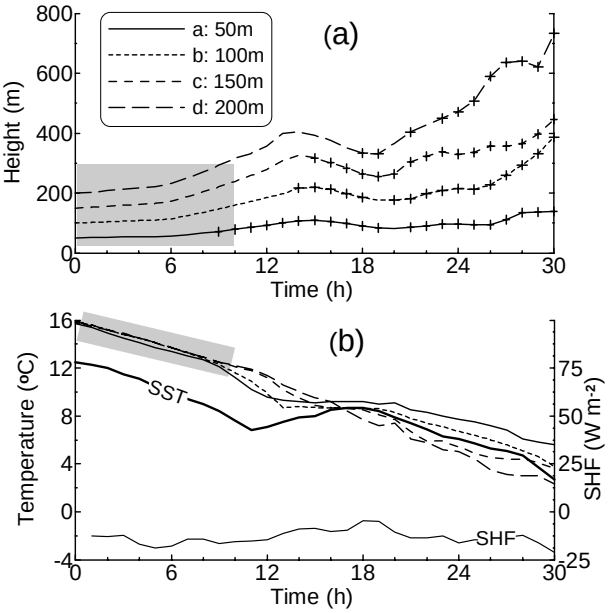

Fig. 15. Temporal changes of (a) air parcels' height (if their relative humidities reach 100%, then symbols "+" are marked) and (b) temperature are shown along the trajectories in Fig. 14. The lines marked SST and SHF indicate changes of SST and sea surface sensible heat flux along the trajectory starting from the height of 50 m.

surface wind speed between both AT minus SST and surface sensible heat flux, respectively, are plotted in Fig. 13. It can be seen from Fig. 13a that favorable AT minus SSTs and wind speeds for this sea fog are 0°–3°C and 2–8 m s^{-1}, respectively. This model statistical result is consistent with previous observations. However, in Fig. 13a there exists an apparent tendency (shown by a dashed line) not pointed out by previous observational analyses. This tendency is that larger AT minus SST corresponds to greater wind speed in the sea fog area. Greater wind speed results in stronger wind shear. The stronger the wind shear is, the stronger the resulting mechanical turbulence will be. More heat will be transported from air to sea in the stable marine layer if mechanical turbulence gets intensified (Fig. 13b). This may explain why larger AT minus SST is not favorable for sea fog formation. For example, if AT minus SST is 5°C, then wind speed will be required to be about 13 m s^{-1} (extend the dashed line in Fig. 13a to estimate this value) to maintain enough heat transport from air to sea, but this wind speed is so strong that it will destroy the stable marine layer and dissipate the sea fog.

The earlier case overview and analysis indicate that persistent southerly wind is an important factor for this sea fog formation. This leads us to view this fog process in a Lagrangian framework. We have calculated a number of trajectories to show the modification of warm air mass as it tracks over the Yellow Sea from south to north. These trajectories represent different air parcels starting at different heights from the same location (see the point "A" in Fig. 14). Figure 15a shows that these parcels slowly increase in height with time when they move northward, and it can be seen apparently that the onset of sea fog first occurs at lower elevations and gradually ascends to higher levels. The onset of sea fog results from cooling because temperature of the whole air mass (shaded in Fig. 15) decreases nearly 4°C (from 16°C to 12°C, see Fig. 15b) during about 10 h. It is obvious that the tendency of this cooling follows the change of the SST. The surface heat flux associated with decreasing SST along the trajectory starting at 50 m indicates that heat is transported from air to sea.

Additional insights can be gained by analysis of vertical cross sections along the line S–N indicated in Fig. 14. Evolution of inversion and sea fog in these vertical cross sections below 1 km are displayed clearly in Fig. 16. As seen in this figure, at 0200 LST 9 March, sea fog began to form (see lower-left corner of Fig. 16a). Figure 16b shows that 6 hours later southerly winds dominated the chosen area and the temperature field obviously changed. The inversion base was elevated from the sea surface and sea fog appeared below the inversion base. The inversion was pushed northward by southerly winds, and the sea fog area followed the movement of the inversion (see Fig. 16c, d). The dissipating of the sea fog is shown in Fig. 16e, f. Cold and strong northerly wind replaced the warm moist southerly wind and lifted the inversion base. The lower part of the sea fog was destroyed while its upper part was lifted (Fig. 16e). Finally, the upper part of the sea fog separated and became stratus cloud (Fig. 16f). To clearly illustrate the relationship between inversion and sea fog, a location (see the point "B" in Fig. 14) is chosen to show their changes with time. In Fig. 17, sea fog is present below the base of the inversion and its height changes, following closely the base. The base of the inversion gradually descends during the first 30 h but gradually ascends later. This descending tendency is rather similar to the changes of the inversions at Sheyang, Qingdao and Chengshantou mentioned previously (Fig. 9). It is obvious that this change results from the warm mass passing through the location (Fig. 16).

Through contrasting Fig. 16a with Fig. 16b and Fig. 16c with Fig. 16d, respectively, we can clearly see that the sea fog area in Fig. 16b is associated with a small AT minus SST (about 2°C) and an inversion exhibiting a value of 4°C in 200 m 6 h previously (Fig. 16a; fog not yet formed), and that southern part of

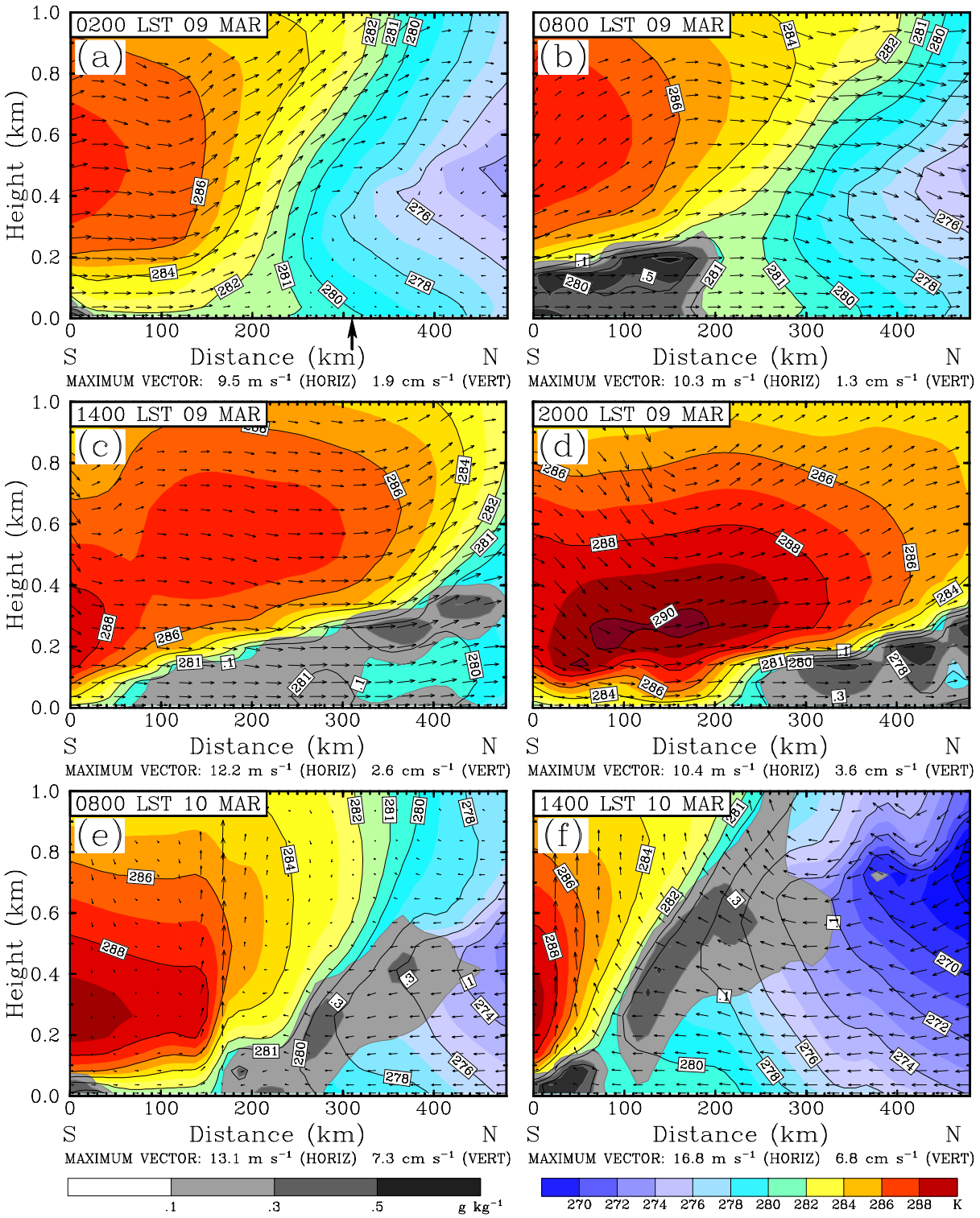

Fig. 16. Vertical sections of wind (vectors), temperature (colorful shading) and cloud liquid water (grey shading) along the line S–N in the control experiment. The arrow in (a) indicates the location B shown in Fig. 14.

Table 1. List of sensitivity experiments.

Experiment	Specification
Sen-Expt1	18-km and 6-km horizontal resolutions
Sen-Expt2	33 full-sigma vertical levels*
Sen-Expt3	45 full-sigma vertical levels**
Sen-Expt4	MODIS weekly SST with 36-km resolution from NASA
Sen-Expt5	SST decreased by 0.5°C
Sen-Expt6	SST increased by 0.5°C
Sen-Expt7	Gayno-Seaman PBL scheme (Stauffer et al., 1999)
Sen-Expt8	Eta PBL scheme (Janjic, 1994)
Sen-Expt9	FNL initial and lateral conditions

Notes: MODIS: Moderate Resolution Imaging Spectroradiometer. NASA: National Aeronautics and Space Administration. FNL: Global Final Analyses of the National Centers for Environmental Prediction (NCEP).

*Their approximate heights are: 0, 37, 111, 186, 261, 376, 530, 688, 847, 1011, 1218, 1473, 1735, 2005, 2283, 2569, 2915, 3327, 3759, 4214, 4692, 5198, 5735, 6308, 6922, 7584, 8304, 9094, 9969, 10954, 12084, 13414 and 15041 m.

**The upper 35 full-sigma levels are almost the same as the control experiment. The approximate heights of the lower 10 full-sigma levels are: 0, 4, 9, 15, 28, 46, 65, 93, 130 and 158 m.

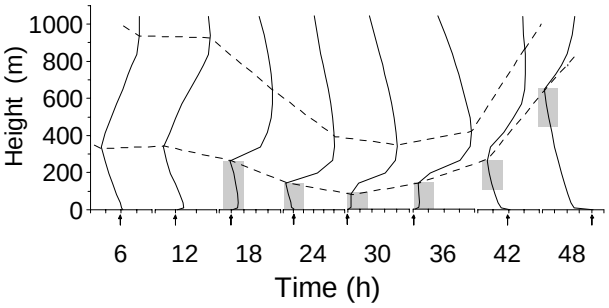

Fig. 17. Vertical temperature profiles with integration time every 6 h at the location B in Fig. 14. The arrows denote 280 K and the interval of temperature is 2 K. The dashed lines indicate the inversion, and shading indicates sea fog/stratus (cloud water mixing ratio more than 0.1 g kg^{-1}).

the sea fog area in Fig. 16c is associated with a large AT minus SST (about 4°C) and a strong inversion exhibiting a value of 6°C in 200 m 6 h later (Fig. 16d; fog already dissipated). This comparison result indicates that a strong inversion corresponding with large AT minus SST is not suitable for sea fog formation (or will dissipate sea fog formed previously).

The region between the inversion base and sea surface can be considered a thermal internal boundary layer (TIBL). Due to the cold sea surface and turbulence mixing, the near-sea-surface air began to cool and the thickness of the cooled air increased with time. Consequently, the inversion base was raised. Comparing the temperature distribution of the TIBL (Fig. 16a–d) with the SST along the line S–N (Fig. 14), it can be judged that the TIBL was a well-mixed layer because its temperature was very near to the SST. Within this well-mixed layer, moistening and cooling by turbulence mixing prompted the sea fog formation. To estimate the height of TIBL varying with downwind distance when a warm air mass passes a cold surface, Garratt (1987) proposed a formula

$$h = 0.014\overline{U}\left(\frac{xT}{g\Delta T}\right)^{1/2}, \qquad (3)$$

where $h, \overline{U}, T, \Delta T, g$ and x are the height of the TIBL, mean wind speed, SST, AT minus SST, acceleration due to gravity and downwind distance, respectively. Here, according to the information in Fig. 16, given values of 10 m s^{-1}, 280 K, 2 K and 9.8 m s^{-2} to $\overline{U}, T, \Delta T, g$ and x, respectively, different h values are calculated to be about 170, 240, 290 and 330 m when the x values are 100, 200, 300, and 400 km, respectively. The top heights of the TIBL in Fig. 16 are quite consistent with these calculated values.

3.3 *Sensitivity experiments*

To test sensitivity of the modeling result to horizontal and vertical resolutions, SSTs, the parameterization of the planetary boundary layer (PBL), and initial and lateral boundary conditions, a series of experiments are performed. Some representative ones are listed in Table 1. The simulated sea fog areas are carefully compared with both the result of the control experiment (CTRL) and GOES-9 images (see Fig. 4). Figure 18 presents the simulated sea fog area and cloud water mixing ratio of these experiments at 1400 LST 9 March.

The resolution sensitivity experiments indicate that higher horizontal and vertical resolutions (Sen-

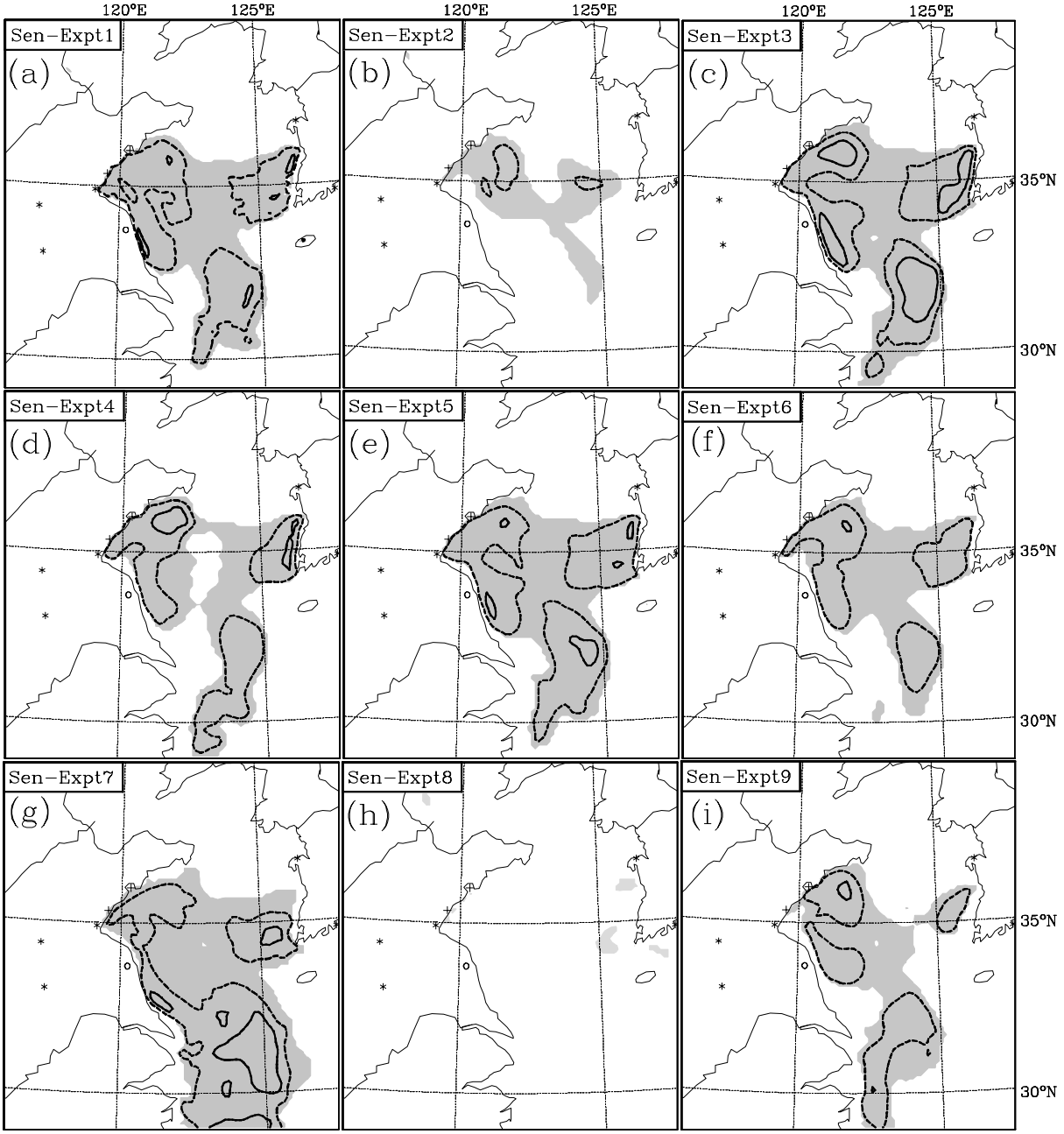

Fig. 18. Simulated fog area (shaded) and cloud water mixing ratio at 10 m (contours; dashed at 0.3 g kg^{-1}, solid at 0.6 g kg^{-1}) of sensitivity experiments at 1400 LST 9 March 2005 (symbols as in Fig. 12).

Expt1, Sen-Expt3) gain some improvement (Figs. 18a, c) while coarser vertical resolution (Sen-Expt2) produces a bad result (Fig. 18b). The simulated sea fog patch in Fig. 18a is closer to the west coast line of the Yellow Sea because the landmask and landuse fields are calculated more accurately in Sen-Expt1. Comparing the heights of vertical levels in Sen-Expt3 with those in CTRL, Sen-Expt3 provides much higher resolution below 200 m than CTRL. Both CTRL and Sen-Expt3 have quite fine vertical resolution, but the vertical resolution of Sen-Expt2 is rather coarse (12 full-sigma levels below 850 hPa), especially below 200 m (only 4 full-sigma levels). Results of the sensitivity experiments suggest that a sufficiently fine vertical resolution (particularly for the PBL) is vital for MM5 to simulate sea fog, and that given a sufficiently fine vertical resolution it is enough for MM5 to simulate sea fog over the Yellow Sea using a horizontal resolution of about 10 km. However, a higher resolution will be needed if more details about sea fog along the coast

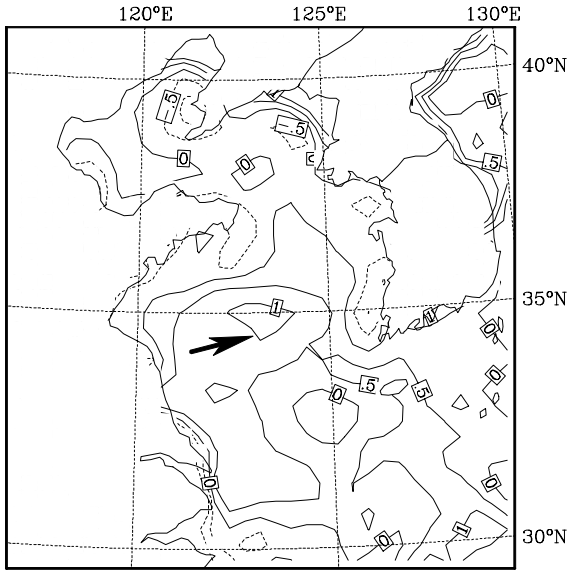

Fig. 19. Difference between SST of Sen-Expt4 and SST of CTRL on 9 March 2005. The bold arrow indicates the area of maximum positive difference.

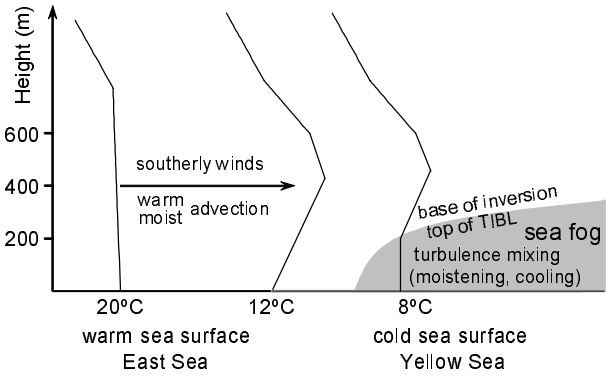

Fig. 20. Schematic illustration of the sea fog. The curves represent temperature vertical profiles over different sea areas, and the corresponding SSTs are also shown below the curves.

are focused on.

The next three experiments (Sen-Expt4, 5, 6) are designed to examine the influence of SST on this sea fog formation and evolution. Figure 19 displays the difference between MODIS weekly SST of Sen-Expt4 and NEAR-GOOS daily SST of CTRL on 9 March 2005. There is an area of maximum positive difference (more than 1°C) that exists in the central Yellow Sea (Fig. 19). A "hole" appears just over this area in the simulated sea fog area of Sen-Expt4 (Fig. 18d). The simulated sea fog area in Sen-Expt5 changes slightly when the SSTs are decreased by 0.5°C. However, reduction of the simulated sea fog area of Sen-Expt6 (SST increased by 0.5°C) is quite great (Fig. 18f, see its "tail" into the East Sea and the concave area on the west coast of the Yellow Sea). These results show that the modeling result is very sensitive to changes in SST.

Other PBL schemes available in MM5 are tested (only the Eta PBL and Gayno-Seaman PBL are listed in Table. 1 and their results are displayed). The high-resolution Blackadar PBL scheme (Blackadar, 1979; Zhang and Anthes, 1982) yields a very similar result to CTRL. The Burk-Thompson PBL scheme (Burk and Thompson, 1989) and Eta PBL scheme yield very poor results (no sea fog is produced, see Fig. 18h). The simulated sea fog area by the Gayno-Seaman PBL scheme is a bit larger (Fig. 18g) than the Hong-Pan PBL scheme used in CTRL. But there is not enough evidence to determine which one is better. Although the Burk-Thompson PBL scheme, Eta PBL scheme and Gayno-Seaman PBL scheme are all based on Mellor-Yamada TKE prediction. The Gayno-Seaman PBL scheme is distinguished from the other two by the use of liquid-water potential temperature as a conserved variable, allowing the PBL to operate more accurately in saturated conditions (Ballard et al., 1991). It seems that the Gayno-Seaman PBL scheme is quite suitable for sea fog simulation. Therefore, more experiments are needed to further evaluate it in future studies.

In Sen-Expt9, FNL reanalyses with finer horizontal and vertical resolutions (1° × 1° resolution and 21 vertical levels from 1000 hPa to 100 hPa) are utilized instead of the JMA analyses. But the result is worse than that of the JMA (Fig. 18i). Comparing the two analyses, it is found that their major differences exist in relative humidities and temperatures within the low level atmosphere, especially near the sea surface.

To further see the PBL structure of each sensitivity run, vertical cross sections (wind, temperature and cloud liquid water) along the line S–N (see Fig. 14) are plotted (not shown). Their wind fields are very similar but the temperature fields below 300 m are so different that cloud liquid water distributions (sea fog) have clear distinctions. For example, the cloud liquid water of more than 0.1 g kg^{-1} is suspended over sea surface at about 50 m height in Sen-Expt8. Since visibility is calculated at 10 m above the sea surface, this leads to such a result as in Fig. 18h.

4. Summary and conclusions

A dense sea fog event that occurred over the Yellow Sea on 9 March 2005 is analyzed and simulated. Its spatial scale (several hundred kilometers) is clearly seen from the NOAA-16 visible image. GOES-9 visible images provide valuable information on its movements.

Analyses of weather situations and observations indicate that this sea fog event has the apparent characteristics of an advection cooling fog.

Further numerical modeling using MM5 basically captures the main features of this sea fog including fog area and its movement. Both location and size of the simulated fog area are consistent with satellite images and its movement agrees with observed visibility very well. The result suggests that it is feasible to simulate sea fog over the Yellow Sea by MM5. Numerical analysis gives us a schematic illustration of this sea fog (Fig. 20). The sea fog formed as a result of modification of the clear marine layer by mechanical turbulence cooling and moistening as it tracked northward over the cold Yellow Sea far from the warm East Sea. This process can be described as follows:

(1) A transient couplet (cyclone/anticyclone) passed over the Yellow Sea during the period 8–11 March. During March 8–9, the Yellow Sea was gradually controlled by the couplet that resulted in southerly winds prevailing over the Yellow Sea.

(2) Southerly winds led to not only water vapor transport but also the movement of the warm air mass already heated by the warm East Sea. Consequently, a strong sea-surface-based inversion formed when the warm air mass tracked over the southern region of the Yellow Sea with cold SST.

(3) Mechanical turbulence mixing by wind shear played an important role. The mixing resulted in not only moistening but also heat transportation from air to sea. This process established a TIBL at the base of the inversion. The sea fog formed and developed within this TIBL and proceeded with its movement.

(4) During 10–11 March, the cyclone of the foregoing couplet was replaced by a strong anticyclone that generated northerly winds over the Yellow Sea. The sea fog was dissipated by the strong cold/dry winds. The formation, development and dissipation of this sea fog were strongly influenced by the transient weather system. Realistic simulation of the transient weather system is a prerequisite for a successful modeling of this sea fog.

In addition, sensitivity tests indicate that the modeling result is significantly affected by employing different PBL schemes and initial and lateral conditions, and SSTs as well. Therefore, it is a challenging task to simulate and predict sea fog, especially for those with small scale along coasts of the Yellow Sea that are extremely sensitive to a number of factors. Progress in data assimilation, dynamics and physics of mesoscale models is making sea fog modeling and prediction hopeful. As we look forward the future of sea fog prediction, probabilistic forecasting using ensemble numerical modeling should be seriously considered.

Acknowledgements. This research was supported by the National Basic Research Program of China (973 program) under Grant No. 2005CB422301. The computation work in this paper was supported by the Ocean University of China Center for High Performance Computing. The authors wish to thank the three reviewers, J. Lewis, D. Koračin and an anonymous one that carefully reviewed the manuscript and made a lot of constructive suggestions for us to improve it. The satellite images, analyses and SSTs used in this paper were all freely downloaded from various websites. Their management agencies, such as Kochi University, JMA, NCAR and NASA, are greatly appreciated.

REFERENCES

Anthes, R. A., E. Y. Hsie, and Y. H. Kuo, 1987: Description of the Penn State/NCAR Mesoscale Model version 4 (MM4). NCAR Tech. Note. NCAR/TN-282+STR., 66pp.

Ballard, S., B. Golding, and R. Smith, 1991: Mesoscale model experimental forecasts of the haar of northeast Scotland. *Mon. Wea. Rev.*, **119**, 2107–2123.

Benjamin, S. G., and N. L. Seaman, 1985: A simple scheme for objective analysis in curved flow. *Mon. Wea. Rev.*, **113**, 1184–1198.

Benjamin, S. B., and P. A. Miller, 1990: An alternative sea-level pressure reduction and a statistical comparison of geostrophic winds estimated with observed surface winds. *Mon. Wea. Rev.*, **118**, 2099–2116.

Bergot, T., and D. Guedalia, 1994: Numerical forecasting of radiation fog. Part I: Numerical model and sensitivity tests. *Mon. Wea. Rev.*, **122**, 1218–1230.

Blackadar, A. K., 1979: High resolution models of the planetary boundary layer. Advances in Environmental Science and Engineering, **1**, 50–85.

Burk, S. D., and W. T. Thompson, 1989: A vertically nested regional numerical prediction model with second-order closure physics. *Mon. Wea. Rev.*, **117**, 2305–2324.

Cho, Y. K., M. O. Kim, and B. C. Kim, 2000: Sea fog around the Korean Peninsula. *J. Appl. Meteor.*, **39**, 2473–2479.

Diao Xuexian, 1996: Main features of sea fog on Qingdao and its neighboring sea areas. *Marine Science Bulletin*, **15**, 87–91. (in Chinese)

Dudhia, J., 1989: A nonhydrostatic version of the Penn State-NCAR mesoscale model. *Mon. Wea. Rev.*, **121**, 1493–1513.

Dudhia, J., 1996: A multi-layer soil temperature model for MM5. Sixth Annual PSU/NCAR Mesoscale Model Users' Workshop, Boulder CO, July 1996, 49–51.

Fan Qi, Wang Anyu, Fan Shaojia, Wu Dui, Deng Xuejiao, and Liu Yingwei, 2003: Numerical prediction exper-

iment of an advection fog in Nanling Mountain area. *Acta Meteorologica Sinica*, **17**, 337–349.

Findlater, J., W. Roach, and B. McHugh, 1989: The haar of north-east Scotland. *Quart. J. Roy. Meteor. Soc.*, **115**, 581–608.

Fu Gang, Wang Jingqian, Zhang Meigen, Guo Jingtian, Guo Mingke and Guo Kecai, 2004: An observational and numerical study of a sea fog event over the Yellow Sea on 11 April 2004. *Journal of Ocean University of China*, **34**, 720–726. (in Chinese)

Fu Gang, Zhang Tao, and Zhou Faxiu, 2002: Three-dimensional numerical simulation of real sea fog event over the Yellow Sea. *Journal of Ocean University of Qingdao*, **32**, 859–867. (in Chinese)

Garratt, J. R., 1987: The stably stratified internal boundary layer for steady and diurnally varying offshore flow. *Bound.-Layer Meteor.*, **38**, 369–394.

Grell, G. A., J. Dudhia, and D. R. Stauffer, 1994: Description of the Fifth-generation Penn State/NCAR Mesoscale Model (MM5). NCAR Tech. Note. NCAR/TN-398+STR., 122pp.

Hong, S. Y., and H. L. Pan, 1996: Nonlocal boundary layer vertical diffusion in a medium-range forecast model. *Mon. Wea. Rev.*, **124**, 2232–2339.

Hu Jifu, Guo Kecai, and Yan Linong, 1996: Discriminate prediction of marine fog occurrence using a model output statistics scheme. *Journal of Ocean University of Qingdao*, **26**, 439–445. (in Chinese)

Hu Ruijin, and Zhou Faxiu, 1997: A numerical study of the effects of air-sea conditions on the process of sea fog. *Journal of Ocean University of Qingdao*, **27**, 282–290. (in Chinese)

Janjic, Z. I., 1994: The step-mountain eta coordinate model: Further developments of the convection, viscous sublayer, and turbulence closure schemes. *Mon. Wea. Rev.*, **122**, 927–945.

Jing Chuancai, 1980: A preliminary analysis of sea fog off the Qingdao coast. *Meteorological Monthly*, **65**, 6–8. (in Chinese)

Klemp, J. B., and D. R. Durran, 1983: An upper boundary condition permitting internal gravity wave radiation in numerical mesoscale models. *Mon. Wea. Rev.*, **111**, 430–444.

Koračin, D., J. Lewis, W. T. Thompson, C. E. Dorman, and J. A. Businger, 2001: Transition of stratus into fog along the California coast: Observation and modeling. *J. Atmos. Sci.*, **58**, 1714–1731.

Kunkel, B., 1984: Parameterization of droplet terminal velocity and extinction coefficient in fog models. *J. Appl. Meteor.*, **23**, 34–41.

Leipper, D., 1994: Fog on the U. S. West Coast: A review. *Bull. Amer. Meteor. Soc.*, **75**, 229–240.

Lewis, J. M., D. Koračin, and K. T. Redmond, 2004: Sea fog research in the United Kingdom and United States. *Bull. Amer. Meteor. Soc.*, **85**, 395–408.

Lewis, J. M., D. Koračin, R. Rabin, and J. Businger, 2003: Sea fog off the California coast. *J. Geophys. Res.*, **108**(D15), 4457, doi:10.1029/2003JD002833.

Mlawer, E. J., S. J. Taubman, P. D. Brown, M. J. Iacono, and S. A. Clough, 1997: Radiative Transfer for Inhomogeneous Atmospheres: RRTM, a validated correlated-k model for the longwave. *J. Geophys. Res.*, **102**, 16663–16682.

Pagowski, M., I. Gultepe, and P. King, 2004: Analysis and modeling of an extremely dense fog event in southern Ontario. *J. Appl. Meteor.*, **43**, 3–16.

Pilié, R., E. Mack, C. Rogers, U. Katz, and W. Kocmond, 1979: The formation of marine fog and the development of fog-stratus systems along the California coast. *J. Appl. Meteor.*, **18**, 1275–1286.

Reisner, J., R. J. Rasmussen, and R. T. Bruintjes, 1998: Explicit forecasting of supercooled liquid water in winter storms using the MM5 mesoscale model. *Quart. J. Roy. Meteor. Soc.*, **124**, 1071–1107.

Stauffer, D. R., R. C. Munz, and N. L. Seaman, 1999: In-cloud turbulence and explicit microphysics in the MM5. *Proc. Ninth PSU/NCAR Mesoscale MODEL User's Workshop*, Boulder, CO, NCAR, 177–180.

Stoelinga, M. T., and T. W. Thomas, 1998: Nonhydrostatic, mesobeta-scale model simulations of cloud ceiling and visibility for an East Coast winter precipitation event. *J. Appl. Meteor.*, **38**, 385–403.

Taylor, G.. I., 1917: The formation of fog and mist. *Quart. J. Roy. Meteor. Soc.*, **43**, 241–268.

Wang Binhua, 1983: *Sea Fog.* China Ocean Press, 352pp. (in Chinese)

Wang Houguang, and Qu Weizhen, 1997: Sea fog prediction for Qingdao area. *Marine Forecasts*, **14**, 52–57. (in Chinese)

Zhang, D. L., and R. A. Anthes, 1982: A high-resolution model of the planetary layer-sensitivity test and comparisons with SESAME-79 data. *J. Appl. Meteor.*, **21**, 1594–1609.

Zhang Hongyan, Zhou Faxiu, and Zhang Xiaohui, 2005: Interannual change of sea fog over the Yellow Sea in spring. *Oceanologia et Limnologia Sinica*, **36**, 36–42. (in Chinese)

Zhao Yongping, Chen Yongli, and Wang Pigao, 1997: Analysis of atmospheric and oceanic conditions for marine fog formation over the Yellow Sea and east China Seas. *Studia Marina Sinica*, **38**, 69–79. (in Chinese)

Zhou Faxiu, Wang Xin, and Bao Xianwen, 2004: Climatic characteristics of sea fog formation of the Huanghai Sea in spring. *Acta Oceanologia Sinica*, **26**, 28–37. (in Chinese)